# Journal of Materials Chemistry C

## Materials for optical and electronic devices

www.rsc.org/MaterialsC

Volume 1 | Number 31 | 21 August 2013 | Pages 4607–4786


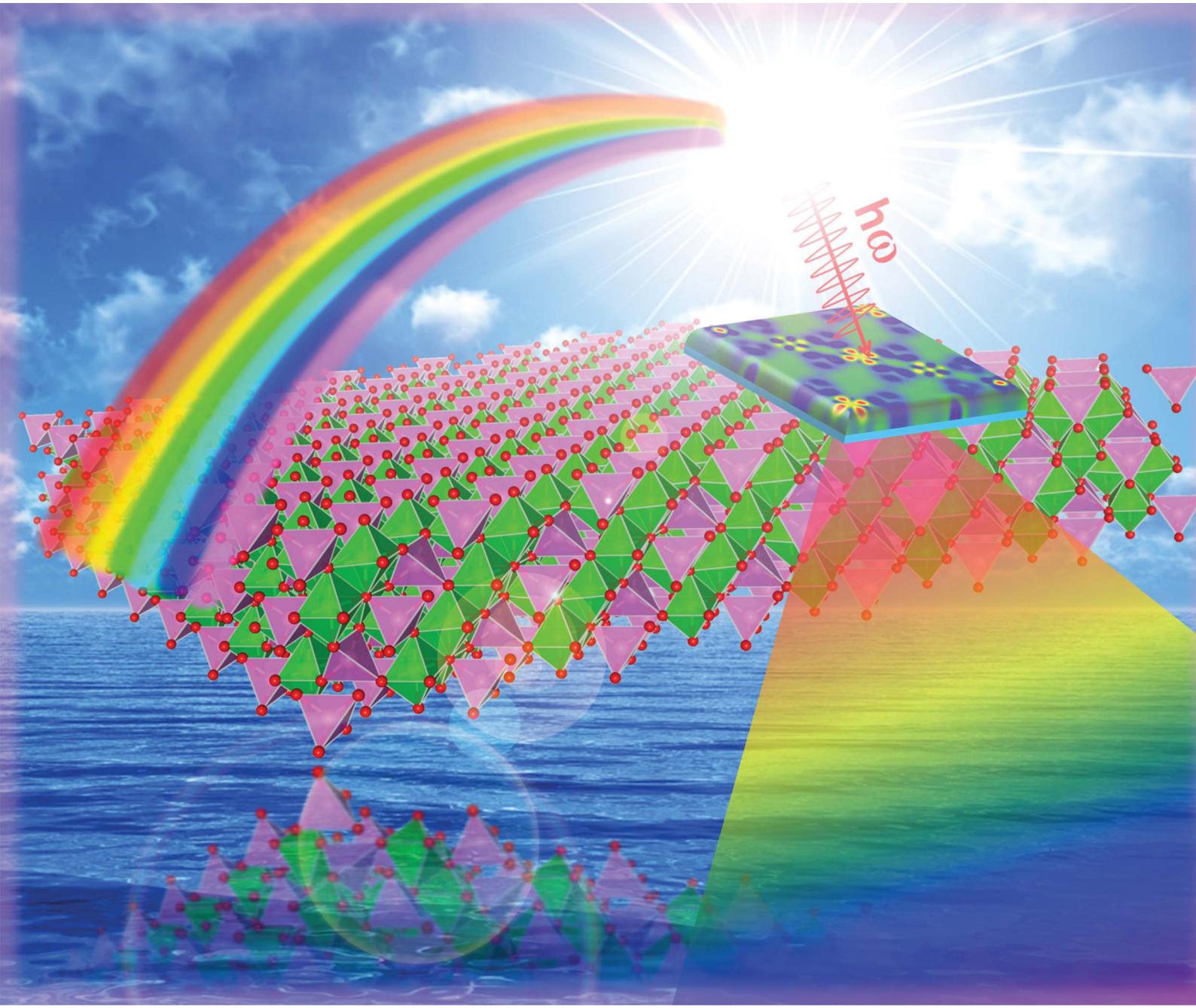



ISSN 2050-7526

RSC Publishing


**COMMUNICATION**

L. Qiao, M. D. Biegalski *et al.*

Nature of the band gap and origin of the electro-/photo-activity of $Co_3O_4$


2050-7526(2013)1:31;1-F

Journal of Materials Chemistry C

RSC Publishing

COMMUNICATION

View Article Online
View Journal | View Issue



Cite this: *J. Mater. Chem. C*, 2013, **1**, 4628

Received 8th May 2013
Accepted 19th June 2013

DOI: 10.1039/c3tc30861h

www.rsc.org/MaterialsC

# Nature of the band gap and origin of the electro-/photo-activity of $Co_3O_4$†

L. Qiao,*[a] H. Y. Xiao,[b] H. M. Meyer,[c] J. N. Sun,[d] C. M. Rouleau,[a] A. A. Puretzky,[a] D. B. Geohegan,[a] I. N. Ivanov,[a] M. Yoon,[a] W. J. Weber[b] and M. D. Biegalski*[a]

**$Co_3O_4$ exhibits intriguing physical, chemical and catalytic properties and has demonstrated great potential for next-generation renewable energy applications. These interesting properties and promising applications are underpinned by its electronic structure and optical properties, which are unfortunately poorly understood and the subject of considerable debate over many years. Here, we unveil a consistent electronic structural description of $Co_3O_4$ by synergetic infrared optical and *in situ* photoemission spectroscopy as well as standard density functional theory calculations. In contrast to previous assumptions, we demonstrate a much smaller fundamental band gap, which is directly related to its efficient electro-/photo-activity. The present results may help to advance the fundamental understanding and provide guidance for the use of oxide materials in photocatalysis and solar applications.**

The ever-increasing needs of global energy exploration demand alternative energy conversion and storage systems that are clean, efficient, and renewable. Spinel $Co_3O_4$ has recently been shown to exhibit remarkable photo- and electro-chemical properties as well as an excellent stability during oxygen reduction and evolution reaction processes.[1–6] These properties, combined with its cost effectiveness and wide abundance, have promoted this material as a promising candidate for fuel cell, lithium ion batteries, water splitting and artificial photosynthesis energy applications. However, despite its promise,[7,8] the basic electronic structure of $Co_3O_4$ that is responsible for these intriguing materials properties is poorly understood both experimentally and theoretically. Particularly, the nature and size of the fundamental band gap[9–18] as well as the origin of the various optical excitations that cover the entire solar spectrum are still under serious debate.[12,19–25] These discrepancies are major barriers that limit the potential of this material for important energy applications, and most likely result from the lack of a comprehensive understanding of its intrinsic optical properties and the absence of a reliable theoretical method for the description of its structure and properties.

In this work, we address previous issues with the electronic structure through the use of phase pure, single crystalline, epitaxial thin films of $Co_3O_4$ (see the ESI, Fig. S1†), coupled with an examination of the optical and electronic properties across a broad wavelength range extending deep into the NIR, to create an accurate model for the first-principle simulation of its structure and properties. For the first time, we clearly demonstrate that $Co_3O_4$ exhibits a fundamental band gap of ~0.74 eV, much smaller than the generally accepted values (*e.g.* from 1.5 to 2.5 eV (ref. 9–18)) and this gap originates from a direct dipole-forbidden d–d transition between tetrahedral-site $Co^{2+}$ cations. Our results lead to a full description of the electronic structure of $Co_3O_4$, and reveal that it is not a highly correlated material. These discoveries, coupled with its strong light absorption across the solar spectrum and p-type semiconducting nature, directly account for its excellent efficiency in various electro-/photo-related chemical processes and provide new insights for designing novel nano- and hetero-structures for energy applications. More importantly, we present a universal combined experimental and theoretical approach to unveil the details of the complicated electronic structures and optical properties of complex oxides, which can be extended to other multiband materials exhibiting complex optical absorptions.

High-quality relaxed epitaxial $Co_3O_4$ films were grown on $Al_2O_3$(0001), MgO(001) and $SrTiO_3$(001) substrates by pulsed laser deposition from high-purity (99.9985%) stoichiometric $Co_3O_4$ targets. Films were deposited with a 248 nm excimer laser source with an energy density of 1.5 J $cm^{-2}$, at a substrate temperature of 600 °C, and an oxygen partial pressure of 200 mTorr, and were cooled down to room temperature in

[a]*Center for Nanophase Materials Sciences, Oak Ridge National Laboratory, Oak Ridge, TN 37831, USA. E-mail: qiaol@ornl.gov; biegalskim@ornl.gov*

[b]*Department of Materials Science and Engineering, University of Tennessee, Knoxville, TN 37996, USA*

[c]*Materials Science and Technology Division, Oak Ridge National Laboratory, Oak Ridge, TN 37831, USA*

[d]*J. A. Woollam Co., Inc., 645 M Street, Lincoln, NE 68508, USA*

† Electronic supplementary information (ESI) available. See DOI: 10.1039/c3tc30861h

200 Torr pure oxygen. The structure and quality of the epitaxial films were determined by reflective high-energy electron diffraction, X-ray diffraction and atomic force microscopy. The electronic and optical properties of the films were characterized by X-ray photoemission, optical absorption, photoluminescence, photoluminescence excitation, and ellipsometry.

Density of states (DOS) and band structures were studied by density functional theory (DFT) calculations using generalized gradient approximation with a Perdew–Burke–Ernzerhof function based on the Vienna Ab initio simulation package.[26] A Hubbard $U$ correction for the on-site Coulomb interaction was considered, with effective $U$ values ranging from 0 to 6 eV for both Co ion species. All calculations included spin-polarization, in which an antiferromagnetic high-spin structure for the tetrahedral $Co^{2+}$ ion and a nonmagnetic low-spin structure for the octahedral $Co^{3+}$ ion were employed. An $8 \times 8 \times 8$ $k$-point sampling in reciprocal space and a plane-wave basis set with an energy cutoff of 500 eV were used and the total energy was minimized to ensure the force on each ion was converged to less than 0.01 eV $Å^{-1}$.

The optical absorption coefficient ($\alpha$) for a 17 nm epitaxial $Co_3O_4$ film was measured within a wide photon energy range between 0.45 and 6.2 eV to include the NIR optical response,[27] as shown in Fig. 1(a). Four distinct absorption bands were clearly revealed with threshold energies of 0.7, 1.6, 2.2, and 4.4 eV. The lowest energy transition band exhibited three peaks, as marked in Fig. 1(b). At a higher energy there was a steep increase in the absorption with a second pronounced band at 1.6 eV. This sharp peak exhibited a highly asymmetric lineshape, indicative of multiple absorption bands. For energies above 2.2 eV, the two absorption bands were much stronger in intensity and broader than the first two, and clearly exhibited visible knee-like features at 3.7 and 4.6 eV. Based on our previous approach,[28] the overall absorption spectrum can be well fitted by a convolution of nine Gaussians accounting for the film absorption (peaks 1–9), one Gaussian for the substrate contribution (peak 10), and a broad low-energy feature due to the refractive index mismatches at the air–film and film–substrate interfaces (peak 11). The existence of this extrinsic contribution (peak 11) was further confirmed by ellipsometry measurements (see the ESI, Fig. S2†).

Although $Co_3O_4$ is highly absorbing, it is not a highly anisotropic optical material, because the absorption features for $Co_3O_4(111)$ films on $Al_2O_3(0001)$ are nearly identical with $Co_3O_4(001)$ films grown on $MgO(001)$ or $SrTiO_3(001)$ (see the ESI, Fig. S3†). Thus, in this work we focus on the films grown on $Al_2O_3(0001)$, although similar results were found for different orientations of $Co_3O_4$ grown on other substrates. Based on a line extrapolation of the lowest absorption peak in the Tauc plot of Fig. 1(b), the optical band gap of $Co_3O_4$ was determined to be 0.76 eV. A similar analysis of the stronger, next higher-energy transition would yield a band gap of 1.6 eV consistent with previous data.[15] It is important to note that the lower band gap of 0.76 eV reported here required measurements extending into the NIR. This band gap was supported by infrared photoluminescence (PL) measurements of a ~100 nm thick epitaxial $Co_3O_4$–$SrTiO_3(001)$ at 10 K [Fig. 1(c)]. Under excitation by a 404.5 nm laser, there was clearly a sharp asymmetric peak at 0.74 eV. This emission does not arise from the substrate, which showed a broad and higher energy peak [Fig. 1(c)]. A similar

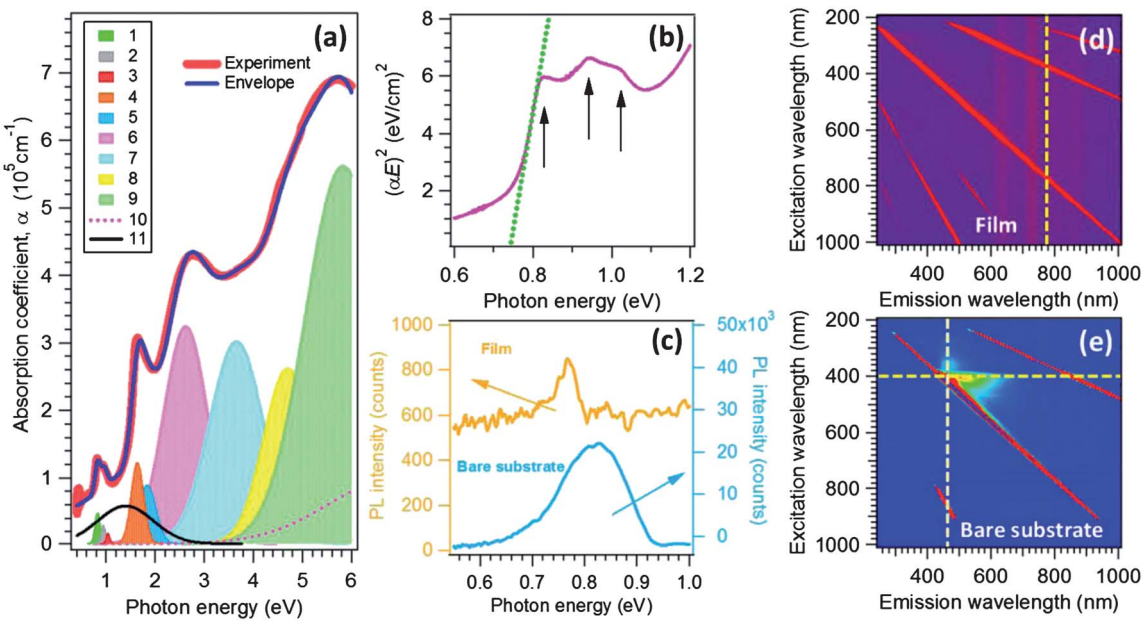


**Fig. 1** Optical absorption and photoluminescence properties. (a) Experimental wide photon energy range optical absorption for a 17 nm epitaxial $Co_3O_4(111)$ film, along with Gaussian peak deconvolutions. The thick red line is the experiment data and the thin blue line is the peak envelope. The optical transition assignments are listed in Table 1. (b) Tauc plot of the same spectrum near the band gap region, where three additional peaks can be seen, as labelled by the black arrows. The band gap of ~0.74 eV was determined by a linear extrapolation of the absorption onset, as indicated by the dotted green line. (c) 10 K PL spectrum of $Co_3O_4$–$SrTiO_3$ and the bare $SrTiO_3$ substrate under a 404.5 nm laser excitation. Photoluminescence excitation spectra mapping for (d) epitaxial $Co_3O_4$–$SrTiO_3$ and (e) the bare $SrTiO_3$ substrate.

low-energy in-gap PL that can be attributed to defects or surface states in the $SrTiO_3$ substrate has also been reported.[29] Based on UV-vis photoluminescence excitation (PLE) spectral mapping [Fig. 1(d) and (e)], it can be seen that the $Co_3O_4$ film does not exhibit any detectable emission near 1.6 eV (~770 nm), where PL might originate if the band gap was in this region (note: there are two emissions from the lamp source at 730 and 620 nm). In addition, the sharp absorption edge and relatively small Stokes shift indicate that the band gap may correspond to a direct-type transition. Though the influences of defect states and substrate effects can not be completely ruled out, the PL emission at 0.76 eV for the $Co_3O_4$ is consistent with absorption, ellipsometry, and is supported in the subsequent arguments through XPS and the following sections, strongly indicating the fundamental band gap is below 1.6 eV.

To clarify the electronic structure of $Co_3O_4$, which contains heterovalent $Co^{2+}$ and $Co^{3+}$ cations, we first compared it to the structure of CoO to separate the electronic structure due to the different valance states of the cobalt ions. Fig. 2(a) and (b) display the Co 2p core-level (CL) and valence band (VB) X-ray photoelectron spectroscopy (XPS) spectra of $Co_3O_4$ and the reference epitaxial CoO, which revealed significant differences between the electronic structures. These differences were demonstrated by the much sharper CL and VB spectra for $Co_3O_4$. Specifically $Co_3O_4$ exhibited a distinctive feature, ②, at the top of the VB with a clear shoulder (feature ③) at a lower binding energy, while CoO exhibited much broader peaks due to multiple splitting from unpaired 3d electrons and p–d charge transfer satellite splitting.[30] To examine these differences in detail, $Co_3O_4$ was sputtered *in situ* using $Ar^+$ in a high vacuum to reduce the surface of the sample to CoO; XPS analysis confirmed the similar broad features of the sputtered $Co_3O_4$ and reference CoO (see the green dotted and blue solid lines). A comparison of the $Co_3O_4$ VB spectra before and after sputtering in Fig. 2(b) revealed an obvious increase in the photoelectron yield near the valence band maximum (VBM), a significant intensity decrease at 1 eV below the VBM, and an intensity increase at higher binding energies. Therefore, the features ① and ③ of $Co_3O_4$ can be ascribed to the $Co^{2+}$ photoelectrons, while the sharp feature ② corresponds to $Co^{3+}$. In addition, the features ④ and ⑤ are ascribed to O 2p and $Co^{3+}$ satellites. These peak assignments partially agree with the work done by Chuang *et al.*[31] and are quite consistent with the cluster calculation results by Jugnet and Duc.[25]

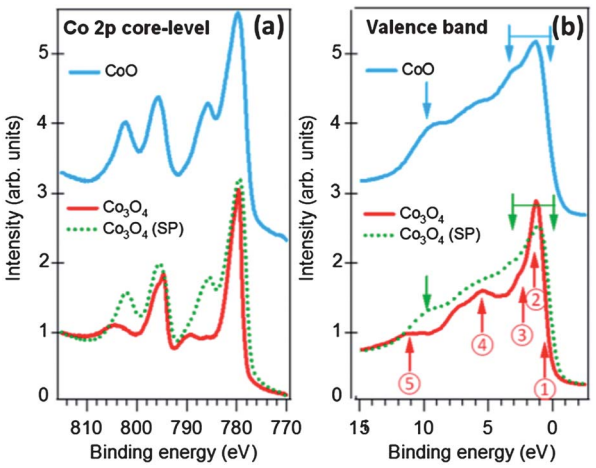


**Fig. 2** *In situ* photoemission spectroscopy. XPS Co 2p core-level (a) and valence band (b) spectra for the $Co_3O_4$(111) and CoO(111) films. The dotted lines are for the $Co_3O_4$(111) film after *in situ* $Ar^+$ sputtering (SP).

With detailed measurements of the electronic structure, first-principle calculations could be employed to determine the electronic fine structures near the Fermi level. The dependency of the total and partial DOS on different effective Hubbard $U$ correction values ($U_{eff}$), for both $Co^{2+}$ and $Co^{3+}$ were calculated and the results are shown as two-dimensional maps in Fig. 3(a)–(d) for the total, $Co^{2+}$ 3d, $Co^{3+}$ 3d, and O 2p orbitals, respectively. Generally, with increasing $U_{eff}$ values for both Co ions, the energy gap between the VBM and the conduction band minimum (CBM) expanded quickly [Fig. 3(a)]. For example, plus $U$ calculations with $U_{eff}(Co^{2+}) > 2$ eV and $U_{eff}(Co^{3+}) > 1$ eV led to a band gap larger than the experimental value of 0.76 eV (see the ESI, Fig. S4a†), and it grew to ~2.2 eV for higher $U_{eff}$ values of $U_{eff}(Co^{2+}) = 4$ eV and $U_{eff}(Co^{3+}) = 6$ eV. For standard DFT, the band gap was smaller than the experimental value due to the well-known DFT underestimation. On the other hand, the increased $U_{eff}$ values led to increasing discrepancies in lattice constants from the experiments, while the differences between DFT + $U$ with small $U_{eff}$ and standard DFT were small (see ESI, Fig. S4b†).

However, the Hubbard $U$ correction with large $U_{eff}$ values introduced remarkable distortions in the electronic structure. When $U_{eff}(Co^{3+})$ exceeded 1 eV, there was a clear discontinuity at the VBM for the total DOS due to the downward bending of the edge corresponding to $Co^{3+}$ 3d orbitals, and this gap was further increased with larger $U_{eff}(Co^{2+})$ values [see the circles in Fig. 3(a) and (c)]. Similarly, when $U_{eff}(Co^{2+})$ exceeded 1 eV, the DOS for the $Co^{2+}$ 3d orbitals was pushed away from the VBM [see the triangles in Fig. 3(b)], which is inconsistent with the photoemission $Co^{2+}$ VBM feature in Fig. 2(b). The calculated total and partial DOS with two extreme combinations of $U_{eff}$ values can be directly compared with the experimental XPS VB spectra in Fig. 4(a) and (d), where the electronic structure distortion caused by the Hubbard $U$ correction can be clearly visualized. Since first-principle methods calculate the ideal DOS distribution at each energy level without considering the actual lifetime broadening of the electron–hole pairs and instrumental broadening of the spectrometer, the calculated DOS was not expected to predict the exact lineshape of the VB. Nevertheless, the calculated energy positions were expected to be close to the experimental values.[32] Note that standard DFT with $U_{eff} = 0$ eV for $Co^{2+}$ and $Co^{3+}$, resulted in a total DOS distribution quite consistent with the experimental VB features at each energy position, as shown in Fig. 4(d). However, in the case of $U_{eff}(Co^{2+}) = 4.4$ eV and $U_{eff}(Co^{3+}) = 6.7$ eV, which have been suggested to reproduce the 1.6 eV band gap,[24] the VB electronic structure was significantly distorted, as shown in Fig. 4(a). Other intermediate $U_{eff}$ value combinations also induced different extents of these VB distortions, as indicated in Fig. 4(b) and (c).

 

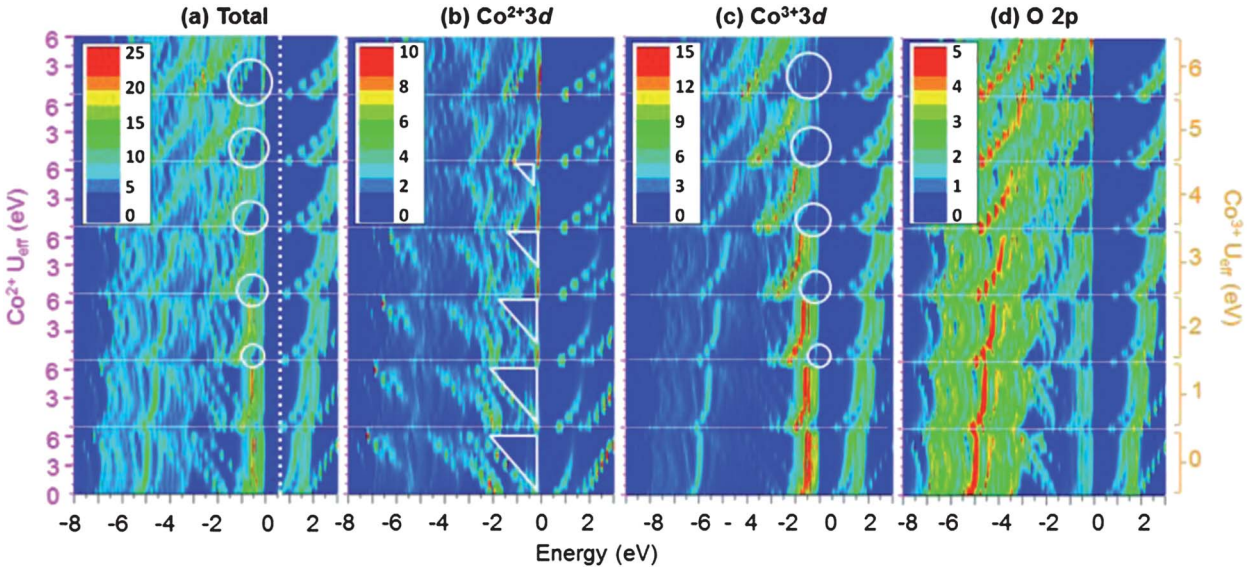


**Fig. 3** DFT calculations under different applied $U_{eff}$ values. Two-dimensional contour mapping of the calculated DOS as a function of different $U_{eff}$ values for both $Co^{2+}$ (left scale) and $Co^{3+}$ (right scale) ions projected onto (a) the total, (b) $Co^{2+}$ 3d, (c) $Co^{3+}$ 3d, and (d) O 2p orbitals. The vertical dotted line in (a) indicates the experimental band gap of 0.76 eV. The intensity scales are labeled in sets.

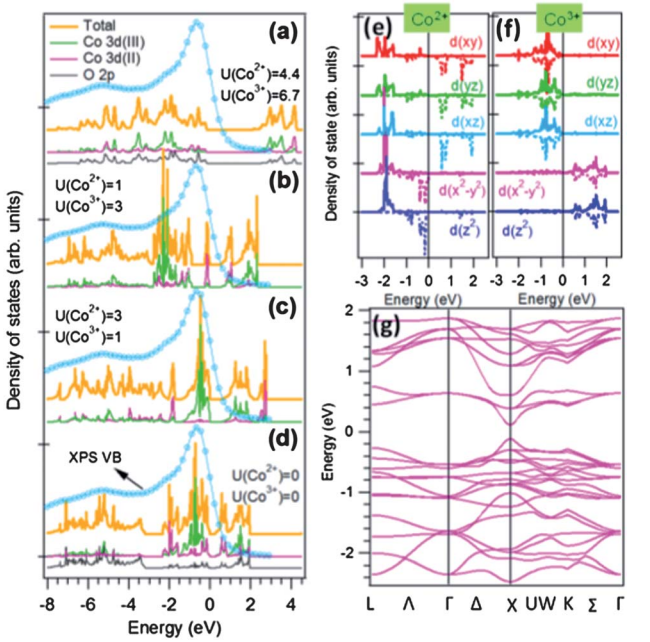


**Fig. 4** Electronic fine structure near the Fermi level. Comparison of XPS VB spectra with the calculated total and partial DOS using (a) suggested $U$ correction for $Co^{2+}$ and $Co^{3+}$ ions by ref. 24, (b) and (c) intermediate $U$ correction and (d) standard DFT. (e) and (f) Calculated orbital-resolved DOS under zero $U$ correction for $Co^{2+}$ and $Co^{3+}$, respectively. (g) Calculated band structure for $Co_3O_4$ under zero $U$ correction.

The electronic structure analysis indicated that, in contrast to CoO, a classic highly correlated Mott insulator, $Co_3O_4$ did not exhibit such strong electron correlations and its electronic structure could be well described by standard DFT. For Mott insulators the conventional DFT failed to describe the strong correlation effects between the d or f electrons and obtained a delocalized electron distribution.[33,34] The Hubbard $U$ correction was thus introduced to localize the orbitals, which were then split into occupied and unoccupied states. For non-Mott insulators, the correction is often used to improve electron localization and the energetic properties. For example, Garcia-Mota *et al.*[35] and Wang *et al.*[36] found that the Hubbard $U$ method yielded a better oxidation energy and formation enthalpy for $Co_3O_4$ than with plain DFT and predicted catalytic properties in good agreement with experiments. Similar cases have also been reported for other transition metal oxides.[37–39] In some cases, the Hubbard $U$ correction may lead to an incorrect electron distribution and a discrepancy from the actual electronic structure. One example is $LaCrO_3$, for which Ong *et al.* revealed that the correction of the correlation effects for the Cr 3d states resulted in an improper electronic structure and a colorless $LaCrO_3$ that contradicted the experimental observation.[40] Therefore, care must be taken in applying the Hubbard $U$ correction to transition metal oxides. Here, in $Co_3O_4$, the Hubbard $U$ correction also caused an improper electronic structure, and the experimental electronic structure and band gap of $Co_3O_4$ agreed well with standard DFT results.

The individual cation–anion orbital distributions near the Fermi level can be resolved from the calculations with $U_{eff} = 0$ eV. The O 2p DOS evolved into two subbands, as shown by a broad and strong band located at $\sim -5$ eV as well as a narrow and weak distribution near the VBM that overlapped with the metal 3d orbitals [see Fig. 3(d) and 4(d)]. A similar hybridization between the metal and ligand also occurred in the CBM. Meanwhile, the cation orbitals also exhibited complicated dispersions in both the occupied and empty states, as revealed by orbital-resolved DOS for both Co cations in Fig. 4(e) and (f). The VBM was primarily occupied by $Co^{2+}$ $e_g$ orbitals with

minority spin and the CBM was occupied by both $Co^{2+}$ $t_{2g}$ orbitals of minority spin and $Co^{3+}$ $e_g$ orbitals with both spin states. The further splitting of the unoccupied states was due to the coupling between the $Co^{2+}$ and $Co^{3+}$ 3d orbitals in the CB. The present results suggest both the orbital hybridization and crystal field effect play important roles in determining the electronic fine structure of $Co_3O_4$.

Based on the obtained electronic fine structure and the energy difference between each orbital, the optical transitions in Fig. 1(a) could be directly assigned, as tabulated in Table 1. The first five transitions from peak 1 to peak 5 are pure d–d type transitions either inside a homovalent Co ion ($Co^{2+}$ or $Co^{3+}$) or between two heterovalent Co ions, depending on the spin orientation. According to the dipole selection rule,[41] d–d transitions would be nominally forbidden for non-hybridized d bands. However, a non-zero transition matrix element between the initial and final states may result from hybridization of the O 2p and Co 3d orbitals, which will lightly relax the parity selection rule and result in a non-zero transition probability. Nevertheless, the matrix element remained small, leading to an absorption intensity orders of magnitude lower than typically allowed transitions. The last four transitions from peak 6 to peak 9 can be attributed to ligand to metal excitations from two types of O 2p subbands to the unoccupied 3d orbitals, for both $Co^{2+}$ and $Co^{3+}$ in the CB. Due to the larger oscillator strength of a p–d type excitation, these transitions are orders of magnitude stronger than the d–d type transitions.[42] We also show in Fig. 4(g) the calculated band structure of $Co_3O_4$. It was found that both the VBM and CBM lie along high symmetry *X* points in the Brillouin zone. As a result, the minimal electronic excitation occurred along this direction without the need of momentum transfer by absorbing or emitting phonons, thus confirming the direct nature of the band gap transition observed with optical spectroscopy. However, the further specification of each band was not possible because of the heavy hybridization among the O 2p, $Co^{2+}$ 3d and $Co^{3+}$ 3d orbitals. The combination of the direct band gap, p-type semiconductivity and highly absorbing nature are responsible for its observed efficiency at light harvesting, electron–hole pair generation and transport upon photon excitation, which explains why $Co_3O_4$ is such an amazing material that exhibits excellent activity in various electro-/photo-related chemical and physical processes.

## Conclusions

In summary, experimental spectroscopy and first-principles calculations were combined to reveal the electronic structure of $Co_3O_4$, which clarified two decades of discrepancies regarding the nature of the band gap and the characteristic optical transitions. We demonstrated evidence of a direct fundamental band gap of 0.76 eV in the NIR that is significantly smaller than previously reported values. The observed electronic excitations were found to originate from the coupling of the crystal field splitting between the tetrahedral and octahedral site cations and from a cation–anion orbital hybridization. It was shown that $Co_3O_4$ did not exhibit a strong electron correlation as compared with the classic CoO and the electronic structure and semiconducting nature of $Co_3O_4$ obtained from standard DFT agreed well with the experimental results. The resolved electronic structure of $Co_3O_4$ illustrated the reason that this material exhibits excellent optoelectronic, photocatalytic, and artificial photosynthesis properties and may assist in the design of nano- and hetero-structured devices based on this material. Finally, the method we demonstrated to resolve the electronic and optical properties of this materials can be extended to the functional properties of other complex transition metal oxides and may help to identify and resolve cases where the electronic structure has been oversimplified.

## Acknowledgements

This research was conducted at the Center for Nanophase Materials Sciences and the SHaRE User Facility, which are sponsored at Oak Ridge National Laboratory by the Scientific User Facilities Division, Office of Basic Energy Sciences, U. S. Department of Energy. H. Y. Xiao and W. J. Weber were supported by the U. S. Department of Energy, Office of Science, Basic Energy Science, Materials Sciences and Engineering Division. The theoretical calculations were performed using the supercomputer resources at the Environmental Molecular Sciences Laboratory (EMSL) located at the Pacific Northwest National Laboratory. H. Y. X. also acknowledges the partial support of the National Natural Science Foundation of China (Grant no. 11004023).

**Table 1** Optical transition assignments for epitaxial $Co_3O_4$ as determined in Fig. 1(a)

| Peak | Energy (eV) | Transitions | Intensity (arb. units) | Type |
|---|---|---|---|---|
| 1 | 0.83 | Co(II) 3d $e_g\downarrow$ → Co(II) 3d $t_{2g}\downarrow$ | 1 | d–d (direct) |
| 2 | 0.95 | Co(II) 3d $e_g\downarrow$ → Co(III) 3d $e_g\downarrow$ | 0.73 | d–d |
| 3 | 1.04 | Co(II) 3d $t_{2g}\uparrow$ → Co(III) 3d $e_g\uparrow$ | 0.33 | d–d |
| 4 | 1.64 | Co(III) 3d $t_{2g}\downarrow$ → Co(II) 3d $t_{2g}\downarrow$ | 6.86 | d–d |
| 5 | 1.84 | Co(III) 3d $t_{2g}$ → Co(III) 3d $e_g$ | 6.92 | d–d |
| 6 | 2.62 | O 2p(I)$\downarrow$ → Co(II) 3d $t_{2g}\downarrow$ | 63.8 | p–d |
| 7 | 3.66 | O 2p(I) → Co(III) 3d $e_g$ | 73.3 | p–d |
| 8 | 4.69 | O 2p(II)$\downarrow$ → Co(II) 3d $t_{2g}\downarrow$ | 51.7 | p–d |
| 9 | 5.8 | O 2p(II) → Co(III) 3d $e_g$ | 192 | p–d |

 

## Notes and references


1 X. Xiao, X. Liu, H. Zhao, D. Chen, F. Liu, J. Xiang, Z. Hu and Y. Li, *Adv. Mater.*, 2012, **24**, 5762–5766.
2 J. Liu, J. Jiang, C. Cheng, H. Li, J. Zhang, H. Gong and H. J. Fan, *Adv. Mater.*, 2011, **23**, 2076–2081.
3 X. W. Lou, D. Deng, J. Y. Lee, J. Feng and L. A. Archer, *Adv. Mater.*, 2008, **20**, 258–262.
4 Y. Liang, Y. Li, H. Wang, J. Zhou, J. Wang, T. Regier and H. Dai, *Nat. Mater.*, 2011, **10**, 780–786.
5 F. Jiao and H. Frei, *Angew. Chem., Int. Ed.*, 2009, **48**, 1841–1844.
6 A. Gasparotto, D. Barreca, D. Bekermann, A. Devi, R. A. Fischer, P. Fornasiero, V. Gombac, O. I. Lebedev, C. Maccato, T. Montini, G. Van Tendeloo and E. Tondello, *J. Am. Chem. Soc.*, 2011, **133**, 19362–19365.
7 M. Haruta, S. Tsubota, T. Kobayashi, H. Kageyama, M. J. Genet and B. Delmon, *J. Catal.*, 1993, **144**, 175–192.
8 W. Y. Li, L. N. Xu and J. Chen, *Adv. Funct. Mater.*, 2005, **15**, 851–857.
9 P. S. Patil, L. D. Kadam and C. D. Lokhande, *Thin Solid Films*, 1996, **272**, 29–32.
10 C. S. Cheng, M. Serizawa, H. Sakata and T. Hirayama, *Mater. Chem. Phys.*, 1998, **53**, 225–230.
11 D. Barreca, C. Massignan, S. Daolio, M. Fabrizio, C. Piccirillo, L. Armelao and E. Tondello, *Chem. Mater.*, 2001, **13**, 588–593.
12 K. J. Kim and Y. R. Park, *Solid State Commun.*, 2003, **127**, 25–28.
13 A. U. Mane and S. A. Shivashankar, *J. Cryst. Growth*, 2003, **254**, 368–377.
14 V. R. Shinde, S. B. Mahadik, T. P. Gujar and C. D. Lokhande, *Appl. Surf. Sci.*, 2006, **252**, 7487–7492.
15 P. H. T. Ngamou and N. Bahlawane, *Chem. Mater.*, 2010, **22**, 4158–4165.
16 A. Louardi, A. Rmili, F. Ouachtari, A. Bouaoud, B. Elidrissi and H. Erguig, *J. Alloys Compd.*, 2011, **509**, 9183–9189.
17 J. G. Cook and M. P. Vandermeer, *Thin Solid Films*, 1986, **144**, 165–176.
18 P. R. Athey, F. K. Urban, M. F. Tabet and W. A. McGahan, *J. Vac. Sci. Technol., A*, 1996, **14**, 685–692.
19 S. Thota, A. Kumar and J. Kumar, *Mater. Sci. Eng., B*, 2009, **164**, 30–37.
20 H. Yamamoto, S. Tanaka and K. Hirao, *J. Appl. Phys.*, 2003, **93**, 4158–4162.
21 M. E. Donders, H. C. M. Knoops, M. C. M. van de Sanden, W. M. M. Kessels and P. H. L. Notten, *J. Electrochem. Soc.*, 2011, **158**, G92–G96.
22 A. Walsh, S. H. Wei, Y. Yan, M. M. Al-Jassim and J. A. Turner, *Phys. Rev. B: Condens. Matter Mater. Phys.*, 2007, **76**, 165119.
23 X. L. Xu, Z. H. Chen, Y. Li, W. K. Chen and J. Q. Li, *Surf. Sci.*, 2009, **603**, 653–658.
24 J. Chen, X. F. Wu and A. Selloni, *Phys. Rev. B: Condens. Matter Mater. Phys.*, 2011, **83**, 245204.
25 Y. Jugnet and T. M. Duc, *J. Phys. Chem. Solids*, 1979, **40**, 29–37.
26 G. Kresse and J. Furthmuller, *Phys. Rev. B: Condens. Matter*, 1996, **54**, 11169–11186.
27 G. J. Exarhos and X. D. Zhou, *Thin Solid Films*, 2007, **515**, 7025–7052.
28 P. V. Sushko, L. Qiao, M. Bowden, T. Varga, G. J. Exarhos, F. K. Urban III, D. Barton and S. A. Chambers, *Phys. Rev. Lett.*, 2013, **110**, 077401.
29 D. Kan, T. Terashima, R. Kanda, A. Masuno, K. Tanaka, S. Chu, H. Kan, A. Ishizumi, Y. Kanemitsu, Y. Shimakawa and M. Takano, *Nat. Mater.*, 2005, **4**, 816.
30 J. van Elp, J. L. Wieland, H. Eskes, P. Kuiper, G. A. Sawatzky, F. M. F. de Groot and T. S. Turner, *Phys. Rev. B: Condens. Matter*, 1991, **44**, 6090–6103.
31 T. J. Chuang, C. R. Brundle and D. W. Rice, *Surf. Sci.*, 1976, **59**, 413–429.
32 P. D. C. King, T. D. Veal, A. Schleife, J. Zuniga-Perez, B. Martel, P. H. Jefferson, F. Fuchs, V. Munoz-Sanjose, F. Bechstedt and C. F. McConville, *Phys. Rev. B: Condens. Matter Mater. Phys.*, 2009, **79**, 205205.
33 G. Kotliar, S. Y. Savrasov, K. Haule, V. S. Oudovenko, O. Parcollet and C. A. Marianetti, *Rev. Mod. Phys.*, 2006, **78**, 865–951.
34 D.-K. Seo, *Phys. Rev. B: Condens. Matter Mater. Phys.*, 2007, **76**, 033102.
35 M. Garcia-Mota, M. Bajdich, V. Viswanathan, A. Vojvodic, A. T. Bell and J. K. Norskov, *J. Phys. Chem. C*, 2012, **116**, 21077–21082.
36 H. F. Wang, R. Kavanagh, Y. L. Guo, Y. Guo, G. Z. Lu and P. Hu, *J. Catal.*, 2012, **296**, 110–119.
37 S. Lutfalla, V. Shapovalov and A. T. Bell, *J. Chem. Theory Comput.*, 2011, **7**, 2218–2223.
38 L. Wang, T. Maxisch and G. Ceder, *Phys. Rev. B: Condens. Matter Mater. Phys.*, 2006, **73**, 195107.
39 J. I. Martinez, H. A. Hansen, J. Rossmeisl and J. K. Norskov, *Phys. Rev. B: Condens. Matter Mater. Phys.*, 2009, **79**, 045120.
40 K. P. Ong, P. Blaha and P. Wu, *Phys. Rev. B: Condens. Matter Mater. Phys.*, 2008, **77**, 073102.
41 F. Wooten, *Optical Properties of Solids*, Academic Press, New York and London, 1972.
42 A. S. Moskvin, A. A. Makhnev, L. V. Nomerovannaya, N. N. Loshkareva and A. M. Balbashov, *Phys. Rev. B: Condens. Matter Mater. Phys.*, 2010, **82**, 035106.

Electronic Supplementary Material (ESI) for Journal of Materials Chemistry C


# Supplementary Information

## Nature of the band gap and origin of the electro-/photo- activity of $Co_3O_4$

L. Qiao[1*], H. Y. Xiao[2], H. M. Meyer[3], J. N. Sun[4], C. M. Rouleau[1], A. A. Puretzky[1], D. B. Geohegan[1], I. Ivanov[1], M. Yoon[1], W.J. Weber[2,3], and M. D. Biegalski[1*]

[1]*Center for Nanophase Materials Sciences, Oak Ridge National Laboratory, Oak Ridge, TN 37831, USA*
[2]*Department of Materials Science and Engineering, University of Tennessee, Knoxville, TN 37996, USA*
[3]*Materials Science and Technology Division, Oak Ridge National Laboratory, Oak Ridge, TN 37831, USA*
[4]*J. A. Woollam Co., Inc., 645 M Street, Lincoln, NE 68508, USA*

### Film epitaxy and structural characterization

Figure **1**a shows x-ray diffraction (XRD) $\theta$-$2\theta$ scan of a 35-nm epitaxial $Co_3O_4(111)$ film on $Al_2O_3(0001)$ substrate. The film exhibits (111) orientation and a fully relaxed structure due the moderate lattice match (~2.2%) between $Co_3O_4[100]$ and $Al_2O_3\,[1\bar{1}00]$. No other impurities, e.g. Co or CoO, are determined indicating a single-phase of the obtained epitaxial film. Notice the epitaxial $Co_3O_4(111)$ exhibits clear thickness fringes around film (222) Bragg peak due to flat film surface and density contrast between film and substrate. The reflective high-energy electron diffraction (RHEED) image show well-defined shape spots along substrate $[1\bar{1}00]$ direction. The presence of both finite thickness fringes and shape RHEED patterns indicate the high quality of the obtained epitaxial $Co_3O_4(111)$ films. Figure **1**b is a high-resolution atomic force microscopy (AFM) image of the film surface. Clear growth-induced step-terrace structure is observed with a minimum height of ~4.6 Å, which corresponds well to the *d*-spacing for a $Co_3O_4$ (111) layer.

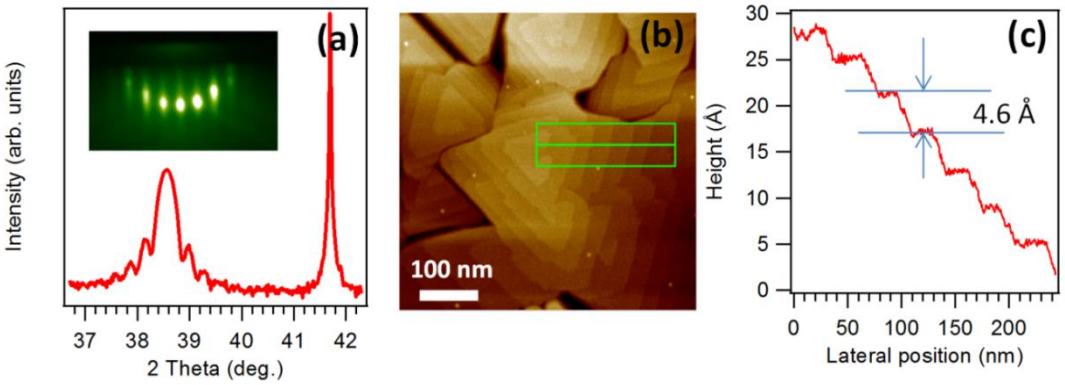


Figure **1** (a) XRD $\theta$-$2\theta$ scan a 35 nm epitaxial $Co_3O_4(111)$ film on $Al_2O_3(0001)$ substrate. Inset shows the RHEED pattern of the film along $[1\bar{1}00]$ crystallographic direction of the $Al_2O_3$ substrate. (b) AFM image of the film surface. (c) Extracted line scan of the rectangular region in AFM image.

## Ellipsometry measurement

Figure **2** shows the determined film refractive index (*n*) and extinction coefficient (*k*). Overall the obtained *k* function mimics the absorption lineshape, e.g. asymmetric peak near 1.6 eV, a broad absorption peak near 2.8 eV, knee-like features at 3.7 eV and 4.5 eV, and a generally increasing trend in absorption for higher energies. These features also qualitatively match the reported complex dielectric function in the literature [1,2]. It is shown that the obtained *n* for film in the low energy range ( < 2.5 eV ), is significantly larger than that of the $Al_2O_3$ substrate, which approaches a constant 1.7 across the whole IR-VIS-UV range [3]. Also, the peak at 1.6 eV determined by ellipsometry is less asymmetric than the same peak in absorption spectrum. Therefore, the broad feature of peak 10 in the absorption measurements originates not from absorption, but from the index mismatches at the various interfaces based on Fresnel theory [4-6]. Similar phenomena have also been reported in other layered organic and oxide systems [7-9].

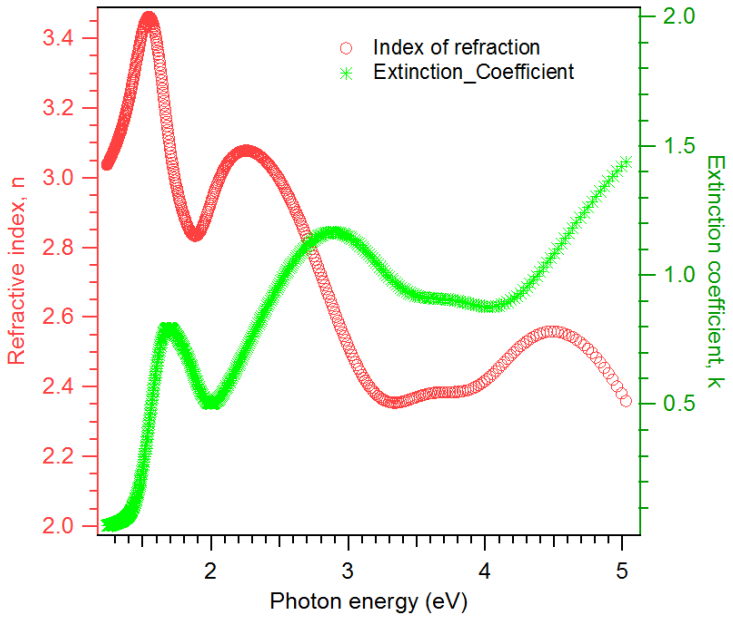


Figure **2** Determined refractive index and extinctive coefficient for epitaxial $Co_3O_4$ film from polarized spectroscopy ellipsometry.

## Substrate choice and optical isotropy of the epitaxial film

The film orientation depends on the choice of substrate. Epitaxial $Co_3O_4$ film exhibits (111) orientation on $Al_2O_3$(0001) substrates, but exhibits (001) orientation on $SrTiO_3$(001) and MgO(001) substrates. We show in Figure **3** the obtained optical absorption spectra for $Co_3O_4$ films grown on different substrates, e.g. 35nm $Co_3O_4$(111) on $Al_2O_3$(0001), 20 nm $Co_3O_4$(001) on $SrTiO_3$(001) and 20 nm $Co_3O_4$(001) on MgO(001) substrates, respectively. It is seen that film absorption is greatly affected by substrate band gap excitation when grown on low band gap substrate $SrTiO_3$ (3.2 eV). Even grown on MgO, which has an intermediate band gap of 7.8 eV, the film absorption is still overlapped with that of the substrate since MgO starts to absorb far below (~5 eV) its nominal band gap. In this case, $Al_2O_3$ is a good substrate choice because of its extreme large band gap (~9 eV), which permits isolation of the film absorption. Comparison of the absorption spectra for $Co_3O_4$(111) and $Co_3O_4$(001) reveals almost identical features, indicating an optical isotropy for this material.

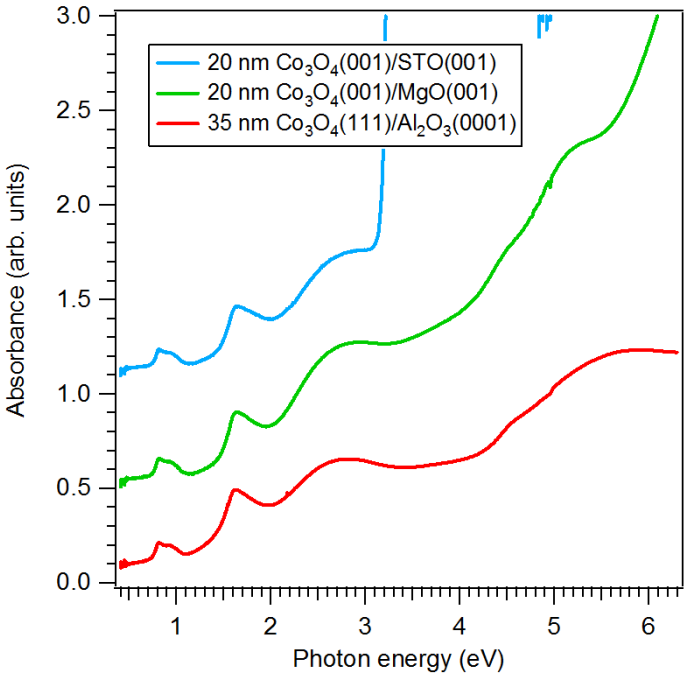


Figure **3**. Room temperature optical absorption spectra for 35nm $Co_3O_4$(111) on $Al_2O_3$(0001), 20 nm $Co_3O_4$(001) on $SrTiO_3$(001) and 20 nm $Co_3O_4$(001) on MgO(001) substrates.

## Effect of Hubbard $U_{eff}$ correction on the band gap and structural properties

We show in Figure **4**a the obtained fundamental gap as a function of different $U_{eff}$ values for both Co ions. Figure **4**b shows the calculated lattice constant as a function of different Hubbard U corrections for both $Co^{2+}$ and $Co^{3+}$ ions. It is seen that zero U correction for both Co ions yields a lattice constant agreeing well with the experimental value, and larger U values for $Co^{2+}$ and $Co^{3+}$ results in increasing deviation of the lattice constant from the experimental one.

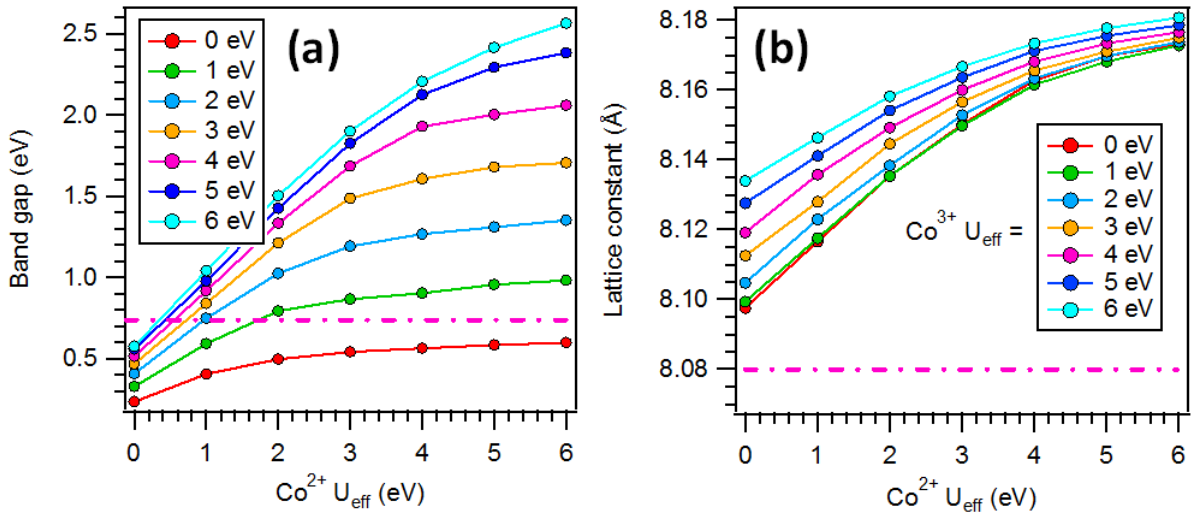


Figure **4**. Calculated band gap (a) and lattice constant (b) as a function of different Hubbard U corrections for both Co ions. Dashed line is the corresponding experimental values.

[1] T. Tanaka, Japanese J. Appl. Phys. 18, 1043 (1979).
[2] J. W. D. Martens et al., J. Phys. Chem. Solids 46, 411 (1985).
[3] R. H. French, H. Mullejans, and D. J. Jones, J. Am. Ceram. Soc. 81, 2549 (1998).
[4] G. A. Boutry, Sci. Prog. 36, 587 (1948).
[5] E. F. C. Driessen, and M. J. A. de Dood, Appl. Phys. Lett. 94, 171109 (2009).
[6] K. Y. Chen et al., Opt. Express 18, 3238 (2010).
[7] A. K. Ray et al., IEE Proc.-Sci. Meas. Technol. 147, 301 (2000).
[8] G. Gaertner, and H. Greiner, in Organic Optoelectronics and Photonics Iii, edited by P. L. Heremans, M. Muccini, and E. A. Meulenkamp (Spie-Int Soc Optical Engineering, Bellingham, 2008), pp. T9992.
[9] P. V. Sushko et al., Phys. Rev. Lett. 110, 077401 (2013).